JOURNAL OF SPACECRAFT AND ROCKETS
Vol. 41, No. 5, September–October 2004

Wake Closure and Afterbody Heating on a Mars Sample Return Orbiter

Thomas J. Horvath,* Nicholas C. Heiner,† and Daniella M. Olguin†
NASA Langley Research Center, Hampton, Virginia 23681

Aeroheating wind-tunnel tests were conducted on a 0.028-scale model of an orbiter concept considered for a possible Mars sample return mission. The primary experimental objectives were to characterize hypersonic near-wake closure and to determine if shear layer impingement would occur on the proposed orbiter afterbody at incidence angles necessary for a Martian aerocapture maneuver. Global heat transfer mappings, surface streamline patterns, and shock shapes were obtained in the NASA Langley Research Center 20-Inch Mach 6 Air and CF_4 Tunnels for postnormal shock Reynolds numbers (based on forebody diameter) ranging from 1.4×10^3 to 4.15×10^5, angles of attack ranging from −5 to 10 deg at 0-, 3-, and 6-deg sideslip, and normal shock density ratios of 5 and 12. Laminar, transitional, and turbulent shear layer impingement on the cylindrical afterbody was inferred from the measurements and resulted in a localized heating maximum that ranged from 40 to 75% of the reference forebody stagnation point heating.

Nomenclature

D	=	aerobrake base diameter, m
d	=	diameter, m
h	=	heat transfer coefficient, $q/(H_{aw} - H_w)$, where $H_{aw} = H_{t,2}$, W/m^2 · K
H	=	enthalpy, kJ/kg
M	=	Mach number
P	=	pressure, N/m^2
q	=	heat transfer rate, W/m^2
R	=	radius, m
Re	=	unit Reynolds number, 1/m
T	=	temperature, K
t	=	time, s
x	=	axial distance along cylinder afterbody, m
α	=	angle of attack, deg
γ	=	ratio of specific heats
θ	=	shear layer turning angle, deg
ρ	=	density, kg/m^3
ϕ	=	cone half-angle, deg

Subscripts

aft	=	vehicle afterbody
eff	=	angular dimension relative to a vector normal to base plane of aerobrake
f	=	forebody
l	=	local condition
n	=	model nose
ref	=	theoretical reference stagnation point heating
s	=	surface quantity, support sting
t, 1	=	reservoir conditions
w	=	wall
2	=	stagnation conditions behind normal shock
∞	=	freestream conditions

Introduction

As the result of a restructured strategy for the exploration of Mars,[1–3] it is anticipated that future robotic missions to Mars will continue to gather scientific data and demonstrate technologies required to address the feasibility of eventually establishing a human presence on Mars. Revisions of the Mars exploration architecture in 2000[4] suggested a sample return opportunity as early as 2011, but this is now considered optimistic. If implemented, a Mars sample return (MSR) mission would collect terrestrial material from the planet surface and return these samples to Earth for detailed analysis. Although missions designed to return samples from Mars have been considered in the past,[5–7] all planetary environmental and surface sample data to date have been acquired from remote-based measurements obtained from the surface or in orbit of Mars. An MSR round-trip mission could require technologies such as aerocapture, precision landing, remote-controlled surface operations including surface material collection, orbital rendezvous, docking, and sample transfer (all at Mars) culminating with a direct entry return at Earth (or shuttle rendezvous).

Before the revised Mars exploration architecture, one approach considered for sample return called for a joint U.S./European MSR mission.[8–11] Key elements of this mission profile are highlighted in Fig. 1. Collected surface samples would be placed into Mars orbit in advance of the arrival of a second vehicle, a French-designed MSR orbiter[12] (MSRO). On planetary approach, the MSRO vehicle would perform an aerocapture maneuver in the Martian atmosphere. With aerocapture, deceleration and orbital insertion is accomplished aerodynamically (in contrast to traditional propulsive techniques) using a blunt aeroshell. After an orbital rendezvous, the material samples would be autonomously transferred to the MSRO and stored in the U.S.-designed Earth entry vehicle[8] (EEV) for the return transit to Earth.

The EEV and the retrieval hardware on the MSRO would reside behind the aeroshell during the aerocapture maneuver before its jettison. Proper positioning of this hardware is essential to ensure aerodynamic stability of the MSRO during aerocapture, to reduce the chances of biological contamination of the EEV(s), and to avoid thermal damage from localized near-wake phenomenon. Although it is generally recognized that convective heating rates to payloads behind aerobrakes are low,[13] localized heating maximum can occur if the boundary layer that separates from the shoulder of the aeroshell impinges on the afterbody.[14–17]

Whereas it is recognized that the hypervelocity entry environment associated with MSR cannot be duplicated in any one ground-based facility, near-wake aeroheating effects due to localized flow impingement are first and foremost the result of the flow physics or fluid dynamic phenomena, for example, boundary layer/shear layer transition, flow separation/reattachment, associated with a given vehicle geometry, attitude, and flight condition. High-temperature chemistry effects at high flow enthalpy levels alter the aeroheating

Received 11 April 2002; revision received 25 October 2003; accepted for publication 25 October 2003.

*Aerospace Technologist, Aerothermodynamics Branch. Member AIAA.
†Cooperative Education Student.

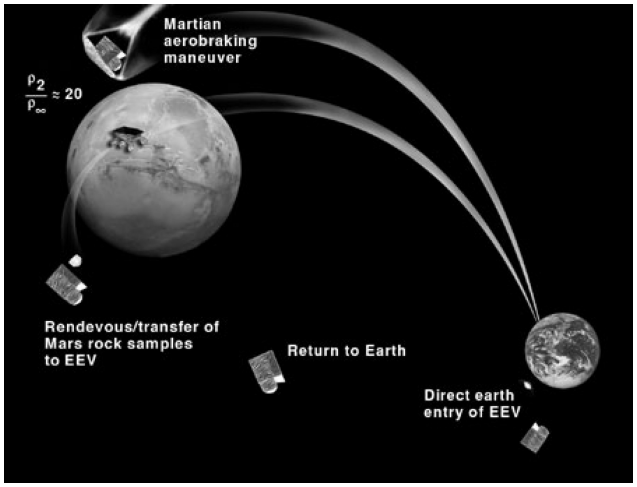

Fig. 1 Major elements of a proposed MSR mission.

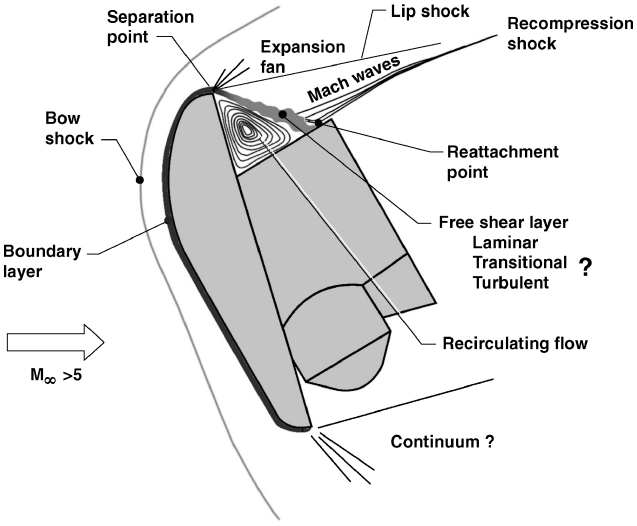

Fig. 2 Schematic of the flow region behind blunt body in hypersonic flow.

characteristics due to flow physics, but do not add new flow physics phenomena, nor delete any. The complexities of blunt-body wake fluid dynamic phenomena (Fig. 2) underscores the potential difficulties in obtaining accurate numerical simulations in this highly separated, expanding/compressing, recirculating flow. Prediction methods that accurately model both blunt-body near-wake flow physics and high-temperature effects are desired to reduce conservative design margins that are often imposed on planetary entry vehicle designs. The primary purpose of the present study was to develop a benchmark experimental laminar and turbulent heating database that captures the blunt-body wake fluid dynamic phenomena under perfect gas conditions. A secondary objective was to investigate the near-wake closure characteristics of the proposed European MSRO vehicle, to determine experimentally whether flow impingement occurred on the MSRO afterbody, and, if present, to determine the location and magnitude of the heating peak under laminar and nonlaminar conditions.

Initial tests in the NASA Langley Research Center 20-Inch Mach 6 CF_4 Tunnel were used to assess laminar MSRO wake closure characteristics because of the facility's ability to provide a low value of the ratio of specific heats and a correspondingly high normal shock density ratios (ρ_2/ρ_∞) of the same magnitude as that incurred in hypervelocity flight. It is anticipated that entry of the MSRO into the atmosphere of Mars (continuum-flow regime) during the aerocapture maneuver will produce values of shock density ratio near 20. (These high values of normal shock density ratio encountered in hypervelocity flight are produced from dissociation of atmospheric gases as they cross through the shock wave into the shock layer and are often referred to as real gas effects.) Flight values of normal shock density ratio are significantly larger (three to four times) than those produced in conventional blowdown hypersonic wind tunnels using air or nitrogen as a test gas.[18] The NASA Langley 20-Inch Mach 6 CF_4 Tunnel utilizes a test gas (tetrafluoromethane CF_4) with a molecular weight 3 times that of air to generate a normal shock density ratio of 12, thereby simulating this particular aspect of a real gas. The simulation is achieved at moderate levels of enthalpy and without dissociation of the test gas. It is well recognized the normal shock density ratio is one of the primary flight simulation parameters that govern the inviscid flow and aerodynamics of blunt bodies at hypersonic speeds.[19] Complementary tests in a perfect gas Mach 6 air facility were later performed over a larger Reynolds number range to assess the effects of shear layer transition on wake closure and impingement heating.

The MSRO was tested at normal shock density ratios of 12 and 5 (in CF_4 and air, respectively) over a range of freestream unit Reynolds number from 3.66×10^3 to 2.44×10^6/m (postshock Reynolds number range based on aeroshell diameter of 1.4×10^3–4.15×10^5). In comparison, a flight trajectory considered by the MSRO program has indicated that the proposed 12-ft-diam aeroshell would experience postshock length Reynolds numbers Re_D of approximately 1.0×10^5 near predicted peak stagnation point heating. Angle of attack was varied from -5 to 10 deg at 0-deg sideslip (limited data at 3- and 6-deg sideslip). Test techniques that were utilized during these tests include thermographic phosphors, which provided global quantitative surface heating images, oil-flow, which provided surface streamline information, and schlieren, which provided shock system details. Emphasis was placed on the afterbody surface heating augmentation due to shear layer impingement.

Experimental Wind-Tunnel Models

The outer mold lines of the proposed MSRO vehicle shown in Fig. 3 represents a reference baseline concept for which experimental and computational wake assessment studies can be conducted. The proposed MSRO vehicle consists of a drag brake and a base-mounted cylindrical afterbody ($d_{\text{aft}}/d_f = 0.48$). The base of the drag brake (aeroshell) is concave inward, as shown in Fig. 3. A single EEV for sample storage and a housing structure for the retrieval/transfer hardware are positioned on the afterbody. The drag brake, or aeroshell, is based on a design[20] originally proposed in support of the aeroassist flight experiment (AFE), a 60-deg elliptically blunted cone with the base raked at a 73-deg angle. At 0-deg angle of attack, the wind vector is aligned with the minor axis of the ellipsoidal nose.

A photograph of two 0.1016-m-diam (0.028-scale) cast ceramic MSRO models used in the test is shown in Fig. 4. For construction of the fused silica models, a rapid prototyping technique was

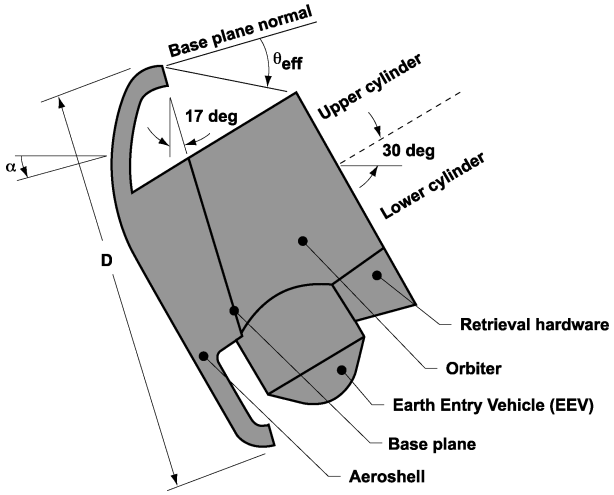

Fig. 3 Proposed MSRO.

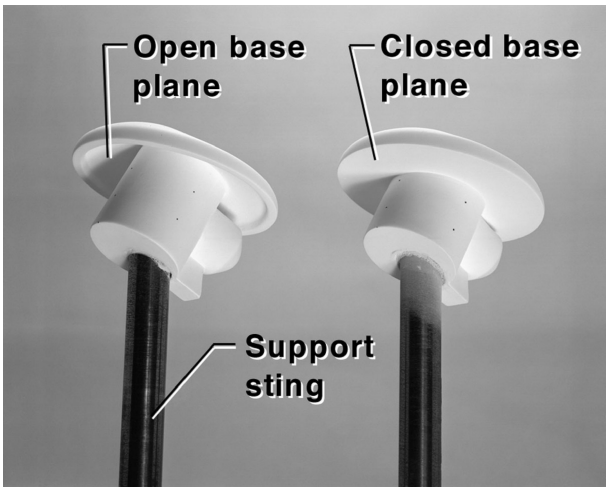

Fig. 4 MSRO Ceramic Heat Transfer Models, 0.028 scale.

utilized. Stereolithography (SLA) was used to build a resin aeroshell model with various detachable SLA afterbodies representing a component buildup of the return orbiter EEV and retrieval/transfer housing structure. The SLA resin aeroshell was then assembled with the desired afterbody; the mated pair served as a pattern to construct molds from which the cast ceramic MSRO models were made. A support sting enters from the rear of the cylindrical afterbody. The aeroshell baseplanes on the MSRO models were constructed both open (concave inward as in Fig. 3) and closed. A photograph of these two base configurations is shown in Fig. 4.

The phosphor coatings that are sprayed on the model surface typically do not require refurbishment between runs in the wind tunnel and have been measured to be approximately 0.0254 mm thick. Details concerning the ceramic model fabrication technique and phosphor coating may be found in Refs. 21 and 22. Fiducial marks were placed on the model surface to assist in determining spatial locations accurately.

Facility Descriptions

Tests were conducted in two facilities managed under NASA Langley Research Center Aerothermodynamic Laboratories (LAL). This complex presently consists of four hypersonic wind tunnels that represent a large fraction of the nation's conventional (low enthalpy) aerothermodynamic test capability.[23] Collectively, they provide a wide range of Mach number, unit Reynolds number, and normal shock density ratio. This range of hypersonic simulation parameters is due, in part, to the use of two different test gases (air and CF_4). The LAL facilities are ideally suited for fast-paced aeroheating and for transition studies aimed at screening, assessing, optimizing, and bench marking (when combined with computational fluid dynamics) planetary vehicle concepts such as the MSRO.

20-Inch Mach 6 Air Tunnel

Heated, dried, and filtered air is used as the test gas. Typical calibrated operating conditions for the tunnel are stagnation pressures ranging from 2.07×10^5 to 3.45×10^6 N/m^2, stagnation temperatures from 422 to 556 deg K, and freestream unit Reynolds numbers from 1.52×10^5 to 2.44×10^6/m. A two-dimensional, contoured nozzle is used to provide nominal freestream Mach numbers from 5.8 to 6.1. The test section is 0.521 by 0.508 m; the nozzle throat is 0.010 by 0.521 m. A bottom-mounted model injection system can insert models from a sheltered position to the tunnel centerline in less than 0.5 s. For the transient heat transfer tests, the model residence time in the flow was limited to 5 s. A detailed description of this facility may be found in Ref. 23.

Mach 6 CF_4 Tunnel

Heated, dried, and filtered CF_4 is used as the test gas. Typical calibrated operating conditions for the tunnel are stagnation pressures ranging from 5.86×10^5 to 1.38×10^7 N/m^2, stagnation temperatures up to 722 deg K, and freestream unit Reynolds numbers from 3.05×10^3 to 1.25×10^5/m. A contoured axisymmetric nozzle is used to provide nominal freestream Mach numbers from 5.9 to 6.2. The nozzle exit diameter is 0.508 m with the flow exhausting into an open-jet test section; the nozzle throat diameter is 0.012 m. A bottom-mounted model injection system can inject models from a sheltered position to the tunnel centerline in less than 0.5 s. For the transient heat transfer tests, the model residence time in the flow was limited to 5 s. A detailed description of this facility may be found in Ref. 19.

Table 1 Nominal flow conditions for the NASA LaRC 20-Inch Mach 6 Air Wind Tunnel

$Re_{2,D}$, $\times 10^3$	Re_∞/m, $\times 10^6$	M_∞	Test gas	$P_{t,l}$, kPa	$T_{t,l}$, K	ρ_2/ρ_∞
36.7	0.21	5.8	Air	234.4	479	5.23
65	0.37	5.9	Air	441.3	488	5.24
123	0.71	5.9	Air	896.3	501	5.25
173.567	1.01	5.9	Air	1282.4	500	5.26
235.967	1.38	6.0	Air	1765.1	500	5.27
325	1.89	6.0	Air	2564.8	517	5.27
415	2.44	6.0	Air	3309.5	514	5.27

Table 2 Nominal flow conditions for the NASA LaRC 20-Inch Mach 6 CF_4 Wind Tunnel

$Re_{2,D}$, $\times 10^3$	Re_∞/m, $\times 10^6$	M_∞	Test gas	$P_{t,l}$, kPa	$T_{t,l}$, K	ρ_2/ρ_∞
1.42	0.003	6.2	CF_4	420.6	703	12.1
2.51	0.006	6.0	CF_4	565.4	697	11.9
3.946	0.009	6.0	CF_4	813.6	688	11.9
15.727	0.04	5.9	CF_4	2689	672	11.7
30.2	0.07	5.8	CF_4	5150.4	712	11.8
44	0.11	5.9	CF_4	7398.1	693	11.7
52.442	0.12	5.9	CF_4	9059.7	709	11.8

Test Conditions and Setup

Nominal reservoir and corresponding freestream flow conditions for the MSRO test series are presented in Tables 1 and 2. The freestream properties were determined from the measured reservoir pressure and temperature and the measured pitot pressure at the test section. Static pressure in the CF_4 test section that enclosed the open jet were monitored to assess the potential for contraction of the open-jet test core flow with time during any given run. The ratio of projected model frontal area to core flow cross-sectional area for the 0.028-scale model is approximately 0.15.

All models were supported by a cylindrical steel rod (sting), which extended downstream from the model base at a 105-deg incidence angle relative to the forebody baseplane. This was done to align the sting along a computationally predicted wake axis with the model at 0-deg incidence. To determine the sensitivity of the support system on base flow heating, several runs were made with an adapter sleeve placed over the existing sting, which increased the sting to forebody diameter ratio (d_s/d_f) from 0.19 to 0.32. A photograph of the installation in the CF_4 tunnel is shown in Fig. 5.

Test Techniques

Advances in image processing technology that have occurred in recent years have made digital optical measurement techniques practical in the wind tunnel. One such optical acquisition method is two-color relative-intensity phosphor thermography,[22,24] which has been utilized in several aeroheating tests[25–27] conducted in the hypersonic wind tunnels of NASA Langley Research Center (LaRC). With this technique, ceramic wind-tunnel models are fabricated and coated with phosphors that fluoresce in two regions of the visible spectrum when illuminated with ultraviolet light. The fluorescence intensity is dependent on the amount of incident ultraviolet light and the local surface temperature of the phosphors. When fluorescence intensity images are acquired with a color video camera of an illuminated phosphor model exposed to flow in a wind tunnel,

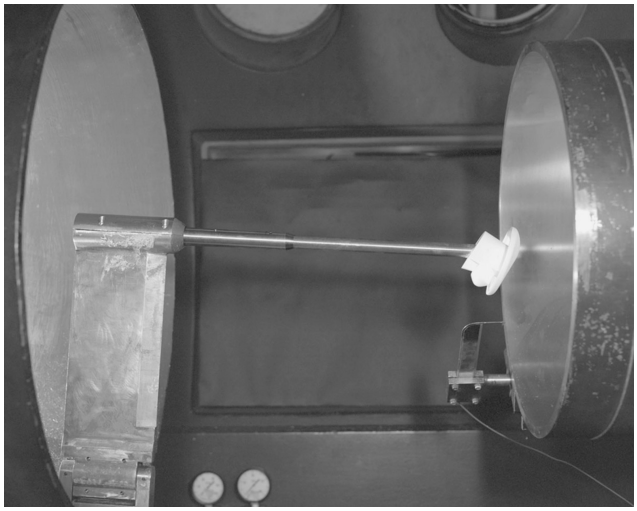

Fig. 5 MSRO heating model installed in the NASA LaRC 20-Inch Mach 6 CF_4 Tunnel.

surface temperature mappings can be calculated on the portions of the model that are in the field of view of the camera. A temperature calibration of the system conducted before the study provides the look-up tables that are used to convert the ratio of the green and red intensity images to global temperature mappings. With temperature images acquired at different times during a wind-tunnel run, global surface heat transfer images are computed assuming one-dimensional semi-infinite heat conduction. The primary advantage of the phosphor technique is the global resolution of the quantitative heat transfer data. Such data can be used to identify the heating footprint of complex, three-dimensional flow phenomena, for example, separation/reattachment, transition fronts, turbulent wedges, boundary-layer vortices, etc., that are extremely difficult to resolve by discrete measurement techniques.

Flow visualization in the form of schlieren photography was used to complement the surface temperature and heating measurements. The LaRC 20-Inch Mach 6 Air and CF_4 Tunnels are equipped with a pulsed white-light, Z-pattern, single-pass schlieren system with a field of view encompassing the entire test core. The light sources are pulsed for approximately a 3 ms. Images were recorded on a high-resolution digital camera and enhanced with commercial software.

Surface streamline patterns were obtained using the oil-flow technique. Backup ceramic models were spray painted black to enhance contrast with the white-pigmented oils used to trace streamline movement. A thin basecoat of clear silicon oil was first applied to the surface, and then a mist of pinhead-sized pigmented-oil drops was applied onto the surface. After the model surface was prepared, the model was injected into the hypersonic flow, and the development of the surface streamlines was recorded with a conventional video camera. The model was retracted immediately following flow establishment (and formation of streamline patterns) and postrun digital photographs were taken.

Data Reduction and Uncertainty

A 16-bit analog-to-digital facility acquisition system was used to acquire flow condition data. Measured values of $P_{t,l}$ and $T_{t,l}$ are believed to be accurate to within $\pm 2\%$.

Heating rates were calculated from the global surface temperature measurements using one-dimensional semi-infinite solid heat-conduction equations.[24] The relative intensity phosphor technique does not necessitate corrections for rolloff angle near the planform edges (such as variable emissivity with an infrared thermography technique). As discussed in Ref. 24, the accuracy of the phosphor system measurement is dependent on the temperature rise of the of the model surface. For the heating measurements, the phosphor system measurement accuracy is estimated to be better than $\pm 8\%$, and the overall experimental uncertainty of the phosphor heating data due to all factors is estimated to be $\pm 15\%$ (including uncertainties in the thermal physical properties of the ceramic material[24]). In areas on the model where the surface temperature rise is only a few degrees, that is, cylinder afterbody, upstream of flow reattachment, the estimated overall uncertainty is on the order of $\pm 25\%$. Repeatability for the normalized centerline (laminar) heat transfer measurements on the afterbody was found to be generally better than $\pm 8\%$. A laser alignment system in the test section and a calibrated precision inclinometer were utilized to set model angle of attack and sideslip; the associated uncertainties are estimated to be ± 0.2 deg.

Heating distributions obtained in $M_\infty = 6$ air and CF_4 along the cylinder afterbody at several time intervals are used to determine when the base flow is established. Although some degree of wake flow unsteadiness is inherent, the shear layer impingement position is typically stable within the framing rate (30 frames/s) and spatial resolution of the schlieren video imagery.

Results and Discussion

Preface

The heating mappings and distributions in the subsequent sections are presented in the form of a normalized heating coefficient h/h_{ref}, where h_{ref} corresponds to the theoretical stagnation point heating at $\alpha = 0$ deg on the model forebody using the method in Ref. 28. The reference radius is 45.97 mm, which approximates the ellipsoidal nose radius of the AFE forebody in the model plane of symmetry. Shear layer turning angle, which is measured relative to a direction normal to the baseplane of the aerobrake (Fig. 3), is inferred from schlieren images, surface streamline patterns, and local heating. Unless indicated otherwise, all data presented were obtained on models with the aeroshell baseplane configured as open (Fig. 4).

Shear Layer Identification

The MSRO is intended to trim between $\alpha = -4$ and $+4$ deg during its aerocapture maneuver at Mars. Schlieren images associated with the MSRO flowfield (in $M_\infty = 6$ air at $Re_{2D} = 4.15 \times 10^5$) are presented in Fig. 6, for a range of angle of attack ($-5 < \alpha < +10$ deg).

In the sequence of images, a weak lip shock associated with the rapid overexpansion and subsequent recompression around the aerobrake shoulder is evident, in addition to a relatively thin free shear layer. Although not attempted in the present study, $M_\infty = 6$ air flowfield surveys in the base region of a similar blunt body[25] have correlated wake lip shock and shear layer boundaries inferred from pitot

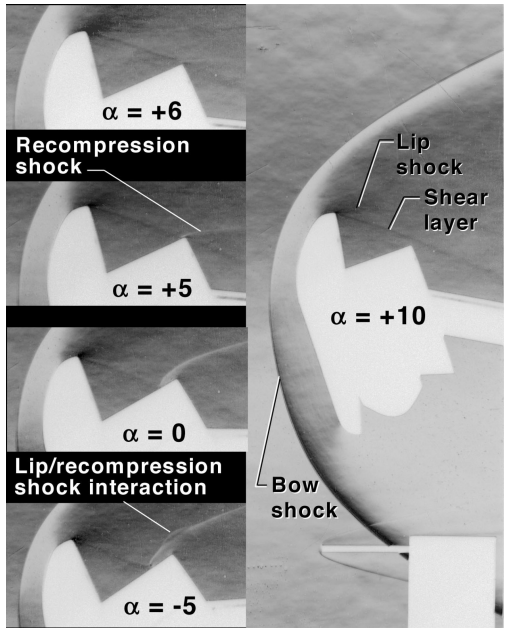

Fig. 6 Schlieren images indicating general flow features observed from MSRO near-wake flowfield: $M_\infty = 6$, air, $Re_{2D} = 4.15 \times 10^5$, and $-5 < \alpha < +10$ deg.

pressure profiles to visual locations inferred from schlieren images. The MSRO schlieren images shown in Fig. 6 indicate that, at angles of attack larger than +6 deg, the afterbody upper symmetry plane (surface opposite the EEV and retrieval hardware) avoids direct shear layer impingement for this condition. As the model angle of attack is decreased, the onset of shear layer impingement is observed to occur (in air) between $\alpha = +6$ and +5 deg and is indicated by a weak recompression shock at the reattachment point near the end of the cylindrical afterbody. The shear layer impingement point progressively moves toward the aerobrake base (and the strength of the recompression shock increases) as the vehicle angle of attack is decreased to $\alpha = -5$ deg. At the limiting incidence angle of $\alpha = -5$ deg, an interaction of the lip shock with the afterbody recompression shock is observed near the aft corner of the afterbody. Shear layer impingement on the EEV and retrieval hardware are not observed in $M_\infty = 6$ air for $-5 < \alpha < +10$ deg. The sensitivity of the schlieren system is insufficient to detect the wake shear layer in the CF_4 facility due to the low density of the base region flow.

Shear Layer Impingement

Shear layer impingement will result in localized surface pressure and convective heating increases. Typical surface streamlines and heating distributions on the MSRO afterbody in the presence of shear layer impingement are shown in Figs. 7 and 8, respectively, at $\alpha = -4$ deg for $M_\infty = 6$ air and $Re_{2D} = 6.5 \times 10^4$. Similar trends were observed at corresponding conditions in $M_\infty = 6$ CF_4. The pressure rise due to reattachment and downstream recompression contributed to the reversal of the flow back toward the open-forebody base as inferred from the surface streamline patterns (Fig. 7). The location of the dividing streamline delineating the entrained recirculating base flow from the flow continuing downstream is evident in Fig. 7. As discussed in a subsequent section, this reversed flow was often observed to produce complex recirculation patterns on the forebody base presumably due to primary and secondary vortices. The corresponding global surface heating pattern (Fig. 8), indicates that the local impingement heating at this condition exceeded 60% of the reference forebody stagnation point value; heating levels upstream of the attachment location and on the base were under 5% of the reference stagnation value. MSRO afterbody flow impingement for sideslip angles up to 6 deg is not observed.

MSRO afterbody wall temperatures in $M_\infty = 6$ air obtained 5 s after model exposure were generally uniform ($T_w = 317$ deg K and $T_w/T_t = 0.61$) in locations away from impingement. At higher Reynolds numbers (discussed later), localized turbulent heating near impingement produced wall temperatures as high as 383 deg K ($T_w/T_t = 0.74$) with peak heating levels that approached 75% of the reference stagnation value.

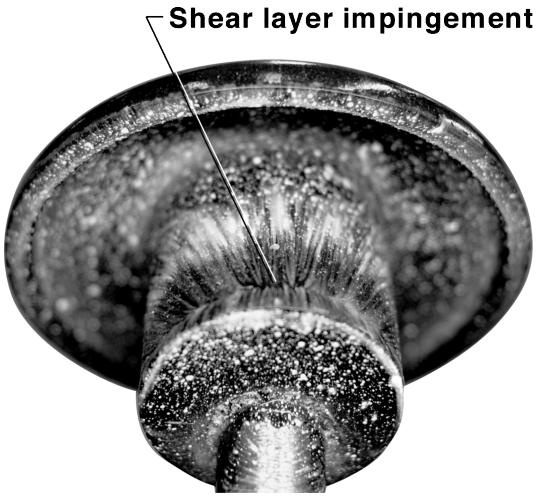

Fig. 7 Typical surface streamlines on MSRO afterbody with open base in the presence of shear layer impingement: $M_\infty = 6$, air, $Re_{2D} = 4.15 \times 10^5$, and $\alpha = -4$ deg.

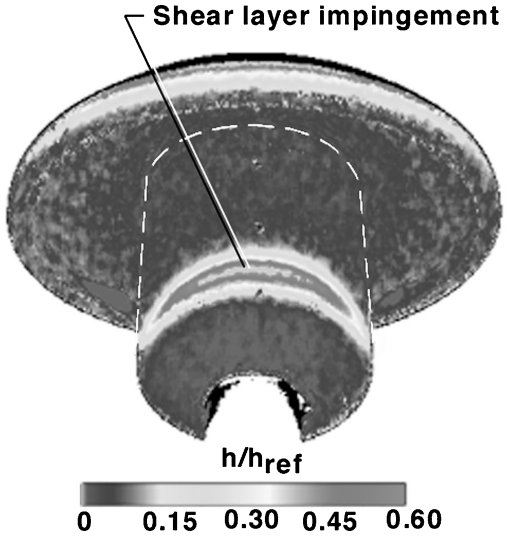

Fig. 8 Typical surface heating on MSRO afterbody in the presence of shear layer impingement: $M_\infty = 6$, air, $Re_{2D} = 4.15 \times 10^5$, and $\alpha = -4$ deg.

Reynolds Number Effects

Because experimental evidence revealed shear layer impingement at trim angles of attack, it became necessary to quantify impingement heating levels and, thus, identify the state of the prevailing interaction (laminar, transitional, or turbulent). As discussed in detail in Ref. 29, separated flows are largely characterized by the prevailing boundary layer or shear layer state. Differences in laminar and turbulent separated regions are primarily attributed to enhanced mixing (greater effective momentum transfer) associated with turbulence. The presence of a transitional shear layer often leads to higher peak heating at reattachment than if the separated flow is entirely laminar or turbulent.[14,30] Whereas edge conditions (Mach number, Reynolds number and γ) at the point of boundary-layer separation determine the initial shear layer turning angle, the state of the interaction (reattachment) downstream also affects the extent (and degree) of unsteadiness of the reversed flow. Thus, a secondary objective of the experimental program was to produce both a laminar and turbulent interaction from which comparisons to numerical solutions could be made. Confidence levels associated with numerical simulation of separated laminar flows are generally lower than for laminar attached flows. As discussed in Ref. 31, the additional complexity of accurately modeling transitional or turbulent separated flow has also proven to be a challenge. (Ironically, it is the laminar wake interaction that is often difficult to achieve in conventional ground-based hypersonic wind tunnel due to facility operational limitations at low Reynolds numbers.)

The $M_\infty = 6$ CF_4 tunnel was initially attractive from the perspective of testing in a gas with a low ratio of specific heats γ, as is encountered in hypervelocity flight. In addition, the facility provides the best opportunity from which to maintain a laminar interaction because it operates at low pressures (and, hence, Reynolds numbers). Normalized heating along the MSRO cylindrical afterbody is shown in Fig. 9 at $\alpha = -4$ deg for $M_\infty = 6$ CF_4 over a range of postnormal shock Reynolds numbers ($Re_{2D} = 1.42 \times 10^3$–$5.2442 \times 10^4$). The abscissa of Fig. 9 (and all subsequent afterbody heating distributions) refers to the running length along the cylinder nondimensionalized by the forebody diameter, which originates at the aft corner and runs forward toward the aerobrake base. The relatively small invariance in the measured magnitude and spatial location of the reattachment heating peak for $Re_{2D} = 1.42 \times 10^3$–$3.946 \times 10^3$ is interpreted as evidence of a laminar interaction. An increase (and subsequent movement) of peak reattachment heating toward the aerobrake base for $Re_{2D} > 3.946 \times 10^3$ suggested a nonlaminar interaction[14,16,32] and/or an increase in the shear layer turning angle. The effects of Reynolds number on shear layer turning angle will be discussed in a subsequent section.

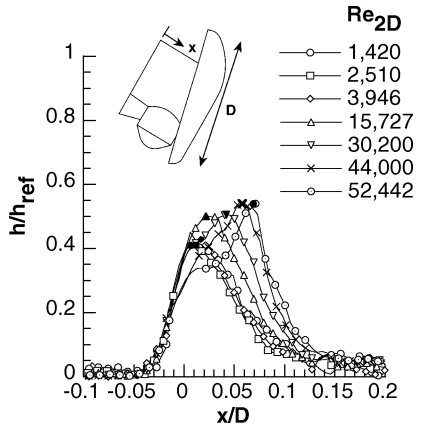

Fig. 9 Effect of Reynolds number on normalized impingement zone heating along MSRO afterbody: $M_\infty = 6$, CF4, $\rho_2/\rho_\infty = 12$, and $\alpha = -4$ deg.

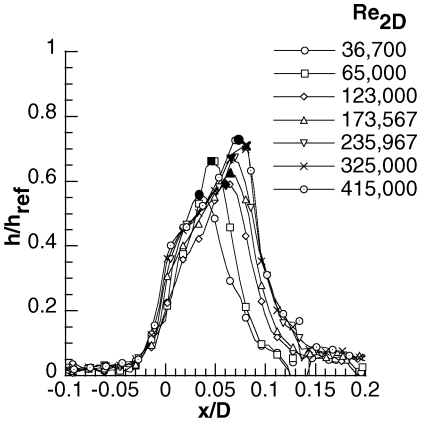

Fig. 10 Effect of Reynolds number on normalized impingement zone heating along MSRO afterbody: $M_\infty = 6$, air, $\rho_2/\rho_\infty = 5$, and $\alpha = -4$ deg.

The $M_\infty = 6$ air tunnel provides an approximate order-of-magnitude increase in postnormal shock Reynolds number over the CF_4 data. Normalized heating along the MSRO cylindrical afterbody is shown in Fig. 10 at $\alpha = -4$ deg in $M_\infty = 6$ air for $Re_{2D} = 3.67 \times 10^4$–$4.15 \times 10^5$. A small overlap in terms of postnormal shock Reynolds number exists between the two facilities. Qualitatively, the magnitude of the measured impingement heating peak in $M_\infty = 6$ air at the lowest Reynolds number ($Re_{2D} = 3.67 \times 10^4$, Fig. 10) is consistent with that measured at the highest Reynolds number ($Re_{2D} = 5.2442 \times 10^4$, Fig. 9) in $M_\infty = 6$ CF_4. The continuation of the forward movement of the local reattachment heating peak in $M_\infty = 6$ air toward the aerobrake base is evident. The continual rise in the heating peak to $h/h_{\text{ref}} = 0.66$, as measured at $Re_{2D} = 6.5 \times 10^4$ and the subsequent drop to $h/h_{\text{ref}} = 0.60$ for $Re_{2D} = 1.23 \times 10^5$ (Fig. 10), is interpreted as the condition at which the transitional shear layer becomes fully turbulent. It is suggested that this situation is analogous to the transitional overshoot phenomenon commonly observed with attached wall boundary layers (where it has been conjectured that the larger vortical length scales associated with transitional flows are more effective at momentum transfer than the finer scales found in a fully turbulent situation). In the postulated turbulent regime, a rise in the nondimensional heating peak to 0.73 for $Re_{2D} = 4.15 \times 10^5$ was measured in $M_\infty = 6$ air. A Reynolds number collapse of turbulent heating data is not observed when normalized with a laminar reference value.

The approximate range of Reynolds number Re_{2D} at which the wake interaction is postulated to go from a laminar to a transitional state, and from a transitional to a turbulent state, is presented in Fig. 11. In Fig. 11, the local heating peak at reattachment has been plotted as a function of Reynolds number Re_{2D} for both $M_\infty = 6$ air and CF_4. The relatively small invariance in the measured magnitude of the reattachment heating peak for $Re_{2D} = 1.420$–3.946×10^3 is interpreted as evidence of a laminar interaction for $M_\infty = 6$ CF_4. The present data suggest a nonlaminar wake for $Re_{2D} > 3.946 \times 10^3$. In perspective, the postnormal shock Reynolds number for Mars entry at peak heating conditions is expected to be near $Re_{2D} = 8.3 \times 10^4$. Although the shear layer transition onset Reynolds number should not be applied directly to flight due primarily to the adverse effect of tunnel noise, the ground-based measurements are considered conservative and suggest the possibility of a nonlaminar wake during the aerocapture maneuver.

A limited literature search yielded several empirically derived correlations[33,34] from which to determine the onset of wake flow transition. It is important to recognize that the presence of a model support sting allows a subsonic path for disturbances to propagate upstream that does not exist in flight. This fact, together with the acoustic disturbance environment present in any conventional tunnel typically results in conservative experimentally derived estimates for wake transition. In a qualitative attempt to classify the present $M_\infty = 6$ CF_4 wake interaction as laminar, the MSRO data are presented in terms of (and compared against) the simple unified wake transition correlation proposed by Ref. 34 in Fig. 12. The parameters for the original correlation in Ref. 34 are freestream length Reynolds number (the length based upon the axial wake transition location relative to the base) and freestream Mach number. The correlation was developed from a large experimental database for cones, spheres, wedges, and sphere–cones that were tested over a range of supersonic and hypersonic Mach numbers. The potential effects of bluntness and body shape on wake transition were recognized in Ref. 34, and the length Reynolds number parameter was modified to include the square of the ratio of the freestream Mach number to a local wake Mach number. In terms of the correlation, the present $M_\infty = 6$ CF_4

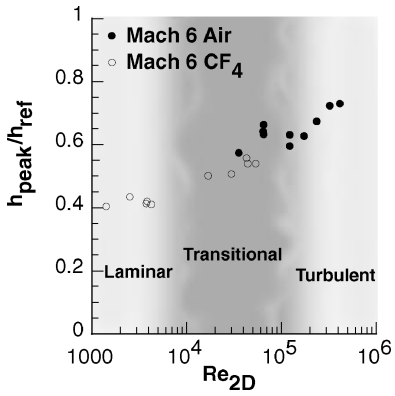

Fig. 11 Effect of Reynolds number on normalized impingement heating peak on MSRO afterbody: $M_\infty = 6$, air and CF_4, and $\alpha = -4$ deg.

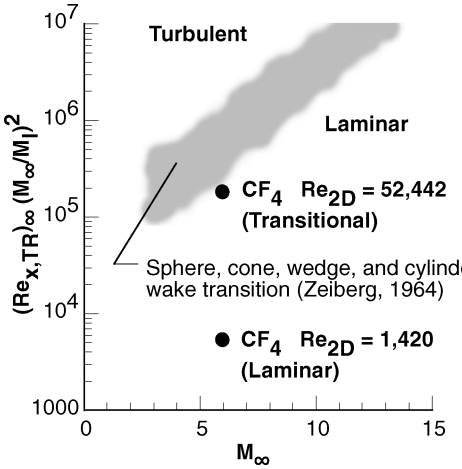

Fig. 12 Comparison of present results to a unified wake transition correlation[34]: $M_\infty = 6$, CF_4, and $\alpha = -4$ deg.

condition (interpreted as laminar for $Re_{2D} = 1.42 \times 10^3$) is an order of magnitude or more below the specified criteria for wake transition. The local wake Mach number for the present results was determined from laminar prediction corresponding to a location just outside of the recirculating base flow (near shear layer impingement). The size of the symbols (Fig. 12), are indicative of the dependence of the correlation parameter to the variation in Mach number as computed in this region. The transition length was assumed to be the axial distance of the aft cylinder (presumably where transition was observed) to the MSRO base. The $M_\infty = 6$ CF_4 results that were interpreted as transitional ($Re_{2D} = 5.2442 \times 10^4$) were significantly closer to the correlation criteria for wake transition.

Base Effects

It is generally recognized that the presence of a support sting will have an effect on the base flow characteristics of a blunt body in hypersonic flow. A limited data set was taken to assess support interference effects. Experimentally, the sensitivity of the MSRO afterbody heating to the potential effects of a cylindrical model support sting was assessed for sting-to-model forebody diameter ratios (d_s/d_f) of 0.19 and 0.32. Figure 13 shows that, at a transitional Reynolds number ($Re_{2D} = 3.67 \times 10^4$) for $M_\infty = 6$ air at $\alpha = -4$ deg, an increase in the support sting diameter produces no measurable effect on impingement location and associated reattachment heating levels. Transitional data for $M_\infty = 6$ CF_4 (not shown) supports a similar conclusion. Comparison of the data in Fig. 13 also serves to indicate the level of repeatability associated with the wake heating measurements.

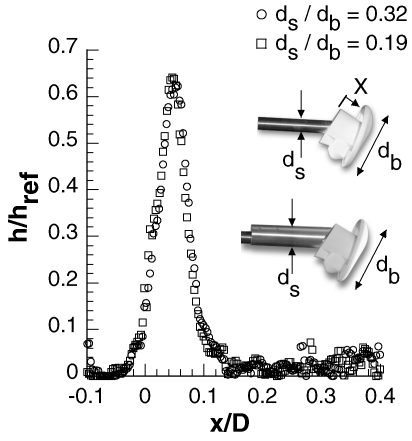

Fig. 13 Effect of support sting diameter on normalized MSRO transitional impingement zone heating: $M_\infty = 6$, air, $Re_{2D} = 3.67 \times 10^4$, and $\alpha = -4$ deg.

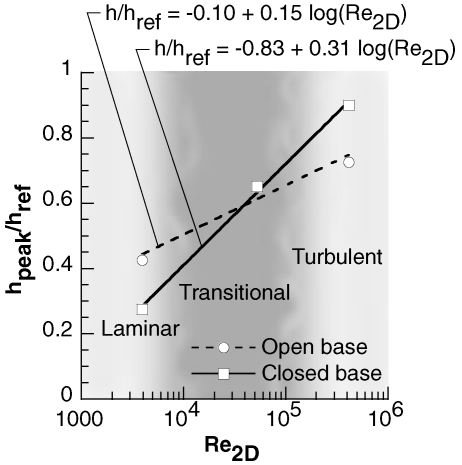

Fig. 14 Effect of open- and closed-MSRO baseplane on normalized impingement zone heating: $M_\infty = 6$ and $\alpha = -4$ deg.

As shown in Fig. 14, the baseplane geometry (open and closed; Fig. 4) and Reynolds number have a pronounced effect on the magnitude of the nondimensional peak heating associated with shear layer impingement on the MSRO afterbody. For a nonlaminar base flow ($Re_{2D} > 3.946 \times 10^3$), reattachment heating increases linearly with the log of the postshock Reynolds number based on body diameter. Logarithmic curve fits to the data plotted in semilog form indicates the rate change of normalized heating associated with the closed base is approximately twice that of the open base. For a laminar wake condition ($Re_{2D} = 3.946 \times 10^3$), in $M_\infty = 6$ CF_4 at $\alpha = -4$ deg, the peak heating associated with the closed (or filled) baseplane is approximately 60% lower (from $h/h_{ref} = 0.43$ to 0.27) relative to that obtained with the open base. In contrast, for a turbulent wake condition ($Re_{2D} = 4.15 \times 10^5$) in $M_\infty = 6$ air, the afterbody peak heating associated with the closed baseplane is approximately 23% higher (from $h/h_{ref} = 0.73$ to 0.90) than that measured with the open base. The turbulent wake associated with the closed MSRO base represents a worst-case scenario in terms of afterbody heating where localized values at reattachment approached forebody stagnation levels. Whereas the reattachment heating levels exhibited a sensitivity to an open or closed baseplane, the spatial location of the heating peak in terms of x/D (and, hence, shear layer turning angle) did not, as shown in Figs. 15–17 for laminar, transitional, and turbulent Reynolds numbers, respectively. The physical explanation of this observation is not clear at the present time, but the increased reattachment heating measured in the absence of increased shear layer turning suggest that the base modifications have produced local flow gradient changes within the shear layer itself that result in increased heating.

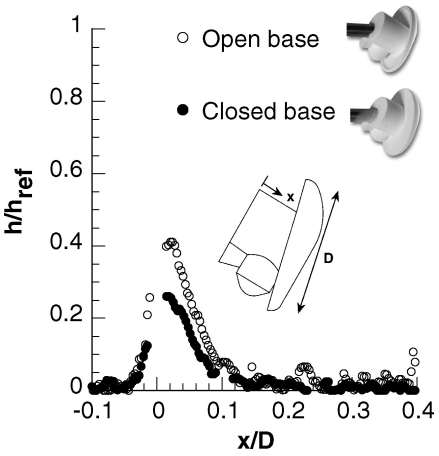

Fig. 15 Effect of open- and closed-MSRO baseplane on normalized laminar impingement zone heating: $M_\infty = 6$, CF_4, $Re_{2D} = 3.946 \times 10^4$, and $\alpha = -4$ deg.

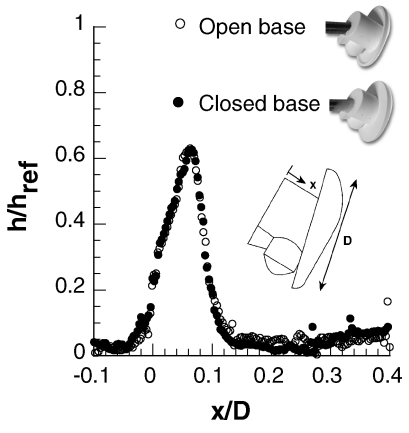

Fig. 16 Effect of open- and closed-MSRO baseplane on normalized transitional impingement zone heating. $M_\infty = 6$, air, $Re_{2D} = 5.2442 \times 10^4$, and $\alpha = -4$ deg.

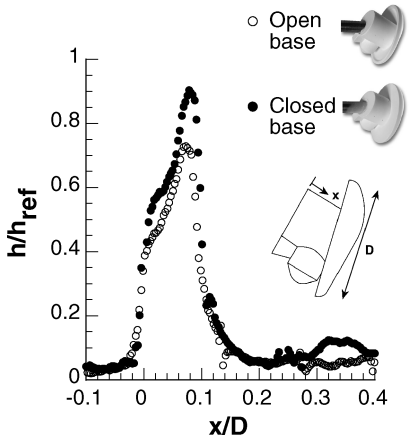

Fig. 17 Effect of open- and closed-MSRO baseplane on normalized turbulent impingement zone heating: $M_\infty = 6$, air, $Re_{2D} = 4.15 \times 10^5$, and $\alpha = -4$ deg.

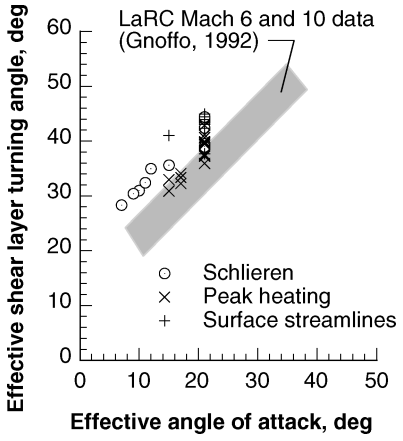

Fig. 18 MSRO shear layer turning angle as a function of effective angle of attack: $M_\infty = 6$, air, and $Re_{2D} = 3.67 \times 10^4$–$4.15 \times 10^5$.

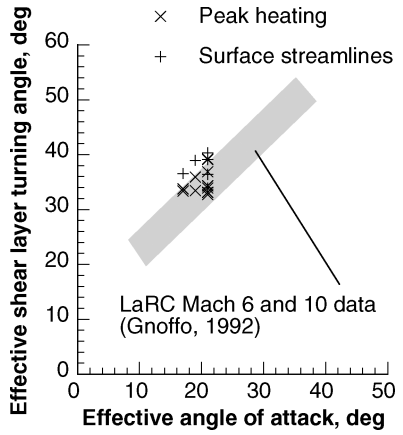

Fig. 19 MSRO shear layer turning angle as a function of effective angle of attack: $M_\infty = 6$, CF_4, and $Re_{2D} = 1.42 \times 10^3$–$5.2442 \times 10^4$.

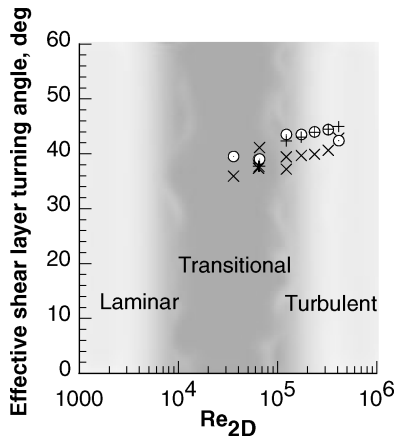

Fig. 20 MSRO shear layer turning angle as a function of Reynolds number: $M_\infty = 6$, air, and $\alpha = -4$ deg: ×, peak heating; ⊙, schlieren; and +, surface streamlines.

Shear Layer Turning Angle Characteristics

From a practical perspective, the usable volume for payload placement behind an aerobrake is generally constrained by the position of the wake free shear layer. The wake boundaries from which the MSRO afterbody was initially designed were inferred from a correlation derived from a series of ground-based blunt-body tests at $M_\infty = 6$ and 10 air and numerical flight prediction.[35] In this correlation, measured and computed shear layer deflection angles and vehicle angle of attack are expressed relative to a direction normal to the given aerobrake baseplane. A linear relationship was identified between the shear layer turning angle θ_{eff} and the effective angle of attack α_{eff}. For the MSRO, α_{eff} is related to the actual MSRO forebody angle of attack through the relationship $\alpha_{\text{eff}} = 17 - \alpha$.

The shear layer turning angle (as a function of effective angle of attack) inferred from the present heating, surface streamline, and shock pattern measurements in $M_\infty = 6$ air and CF_4 are presented in Figs. 18 and 19, respectively. For clarification purposes, the ground-based results from Ref. 35 are presented in Figs. 18 and 19 in the form of a shaded band. Consistent with the methodology of Ref. 35, the shear layer deflection angles are measured by drawing a straight line from the model base corner to the measured location of the attachment point as inferred from surface streamline patterns, schlieren images, and the location of peak heating using phosphor thermography.

The present MSRO results obtained with the open baseplane exhibit the same general linear trend as the correlation of Ref. 35. The turning angle inferred from the CF_4 heating and streamline measurements (Fig. 19) compare well with the correlation. In the present data, the variation of the turning angle for each effective angle of attack has been attributed to transitional/turbulent Reynolds number effects discussed earlier. That is, for a nonlaminar interaction, an increase in Reynolds number moves the impingement location toward the aerobrake base, implying a larger turning angle. The effect of Reynolds number on shear layer turning for a laminar interaction is inconclusive due to the limited range of Reynolds number for laminar CF_4 data. The $M_\infty = 6$ air results (Fig. 18) indicate a bias toward a larger turning angle relative to the original correlation, and this is, in part, attributed to the greater turbulent Reynolds number range achieved in the present tests.

For a given Reynolds number Re_{2D} corresponding to a nonlaminar shear layer, the shear layer turning angle as inferred from surface streamlines or shock patterns is generally greater than that determined via the peak heating location. Shear layer turning angles as a function of Reynolds number Re_{2D} for $\alpha = -4$ deg in $M_\infty = 6$ air and CF_4 are presented in Figs. 20 and 21, respectively. For the laminar $M_\infty = 6$ CF_4 condition ($Re_{2D} = 1.420$–3.946×10^3), the turning angle associated with peak heating on the afterbody is within 1 deg of that inferred from surface streamlines or shock patterns, as shown in Fig. 21. For transitional/turbulent conditions in $M_\infty = 6$ air ($Re_{2D} > 3.946 \times 10^3$; Fig. 20), this difference is as large as 4 deg. As indicated by the data in Figs. 20 and 21, the turning angle for a transitional/turbulent interaction is larger than its laminar counterpart. As inferred from this data, the transitional/turbulent heating maximum on the cylinder afterbody ($Re_{2D} > 3.946 \times 10^3$) is located downstream of the reattachment point as determined from surface streamlines or shock patterns. This difference in location is consistent with the experimental observations of Ref. 17.

In contrast to the current analysis, it was concluded in Ref. 35 that no significant effects due to Reynolds number Re_{2D}, were observed in the ground-based test data that the shear layer turning angle correlation was derived from. In that study however, the Reynolds number range was relatively limited. It was also noted in Ref. 35 that slightly

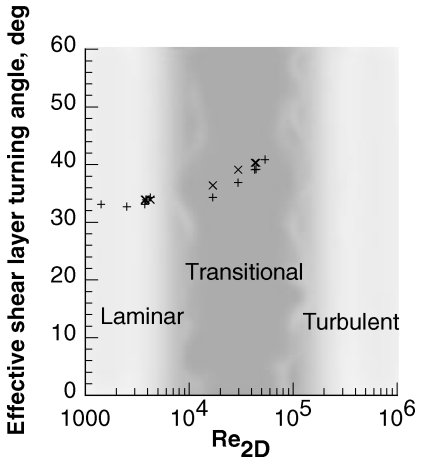

Fig. 21 MSRO shear layer turning angle as a function of Reynolds number: $M_\infty = 6$, CF_4, and $\alpha = -4$ deg: ×, surface streamlines and +, peak heating.

larger shear layer turning angles were predicted at flight conditions relative to low enthalpy ground-based experimental measurement and it was suggested that this could have been a gas chemistry effect. As discussed in Ref. 35, the severe compression in the forebody shock layer and the subsequent rapid expansion into the wake are characterized by high-temperature, thermochemical nonequilibrium processes. It is recognized that the present MSRO simulation tests in CF_4 or air do not duplicate chemical/thermal nonequilibrium effects associated with blunt-body wake flow. Thus, one of the largest unknowns associated with the present ground-based testing is the extrapolation of leeside or wake flowfield characteristics measured in the wind tunnels to flight. Data derived from conventional air facilities regarding leeward flow separation, reattachment, transition of separated or attached leeward flow, and leeward vortex interactions all present significant scaling issues as discussed in Ref. 36. Historically, the CF_4 tunnel has not been heavily utilized for characterization of separated, leeward (or wake) flows, but rather for aerodynamics associated with blunt planetary entry configurations where the inviscid forebody flow is primarily governed by the normal shock density ratio.[37] If in hypervelocity entry, the MSRO near-wake flow is nonreacting or frozen due to the rapid flow expansion around the forebody shoulder, it is quite possible that that the CF_4 simulation (with a freestream $\gamma = 1.22$) will provide a rather good representation of coupled leeside flow physics and flow chemistry. From an aerodynamic perspective, the extrapolation methodology is more clear. In Ref. 38, gamma defined as local enthalpy divided by internal energy was used to characterize successfully the Space Transportation System STS-1 pitch up anomaly by relating orbiter aerodynamic measurements made in the CF_4 tunnel to flight predictions. These tests have shown that the increments and trends provided by real gas simulation tests in air and CF_4 are applicable to flight provided that 1) the vehicle aerodynamics are dominated by the windward surface pressure (shear stress contributions negligible), 2) γ_{eff} within the flight windward shock layer does not significantly vary spatially, and 3) γ_{eff} within the flight windward shock layergs close in magnitude to that produced in CF_4 ($\gamma_{\text{eff}} = 1.1$). Despite ground-based testing simulation issues and geometrical afterbody differences from those configurations used to define the turning angle correlation of Ref. 35, the present MSRO laminar CF_4 data have suggested the general applicability of the correlation for predicting wake shear layer turning for initial design estimates. If shear layer transition in flight is anticipated, that is, via forebody surface ablation or surface roughness, a larger turning angle should be expected.

The intent of the baseline MSRO afterbody design was to avoid impingement at trim angles of attack. The present results along with recent hypersonic tests[12,39] conducted in European facilities (in air and CO_2) have all indicated flow impingement on the MSRO afterbody near trim conditions. Flight computations[10–12] have indicated impingement as well. These experimental and computational results reveal the presence of impingement, which will necessitate the use of a supplemental thermal protection system such as an afterbody shield discussed in Ref. 12 should the afterbody geometry not change. In hindsight, it appears that the early engineering estimates of the MSRO wake closure characteristics (to avoid shear layer impingement) were not conservative enough to account for dispersions. For design purposes, a shear layer turning angle of 30 deg (Fig. 22) was originally assumed based on an effective angle of attack of 15 ($\alpha = +2$ deg) deg. Because aerodynamic performance of the aerobrake during an aeropass maneuver was refined to include dispersions, the effective angle of attack to trim the MSRO was increased to 19 deg ($\alpha = -2$ deg) and later to 21 deg ($\alpha = -4$ deg). Based on the correlation of Ref. 35, the projected shear layer turning angle relative to the baseplane would increase to approximately 39 deg. The relationship of these turning angles relative to the MSRO afterbody is shown in Fig. 22. As inferred from the correlation, impingement on the afterbody would occur for effective angles of attack of 19 and 21 deg.

If shear layer impingement is present at flight conditions and adequate thermal protection is not possible, a small rotation or lateral displacement of the afterbody in the plane of symmetry or scarfing the aft corner could provide a means to avoid impingement as shown in Fig. 23. While possibly mitigating localized heating, afterbody displacement or scarfing would affect the vehicle c.g. location and the MSRO aerodynamics. Alternatively, an appropriate modification to the MSRO base geometry near the MSRO shoulder (Ref. 12) could delay flow separation from the base and prevent local impingement heating to the orbiter afterbody. A computational study in Ref. 40

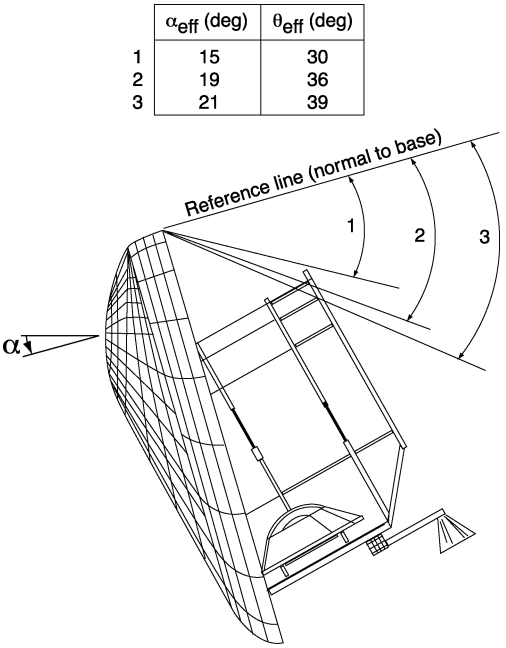

Fig. 22 Estimated position of MSRO wake shear layer relative to the afterbody for various effective angles of attack.

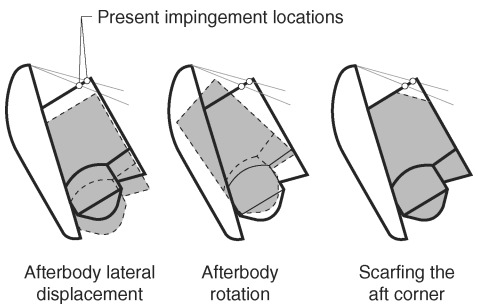

Fig. 23 Potential configuration modifications to avoid shear layer impingement on MSRO afterbody.

investigated the effects of afterbody geometry on wake closure and base heating for a spherically blunted cone. Relative to a cylindrical afterbody, it was determined in Ref. 40 that a conical afterbody moved baseflow separation downstream, thereby eliminating direct shear layer impingement that was present on the cylindrical base. As expected, the acreage heating associated with the conical afterbody was higher relative to that predicted on the cylindrical afterbody. Thus, whereas base modifications may prevent local heating from direct flow impingement, increased acreage heating on the base may result in additional thermal protection and add undesirable mass to the orbiter aft of the vehicle c.g. location.

Blunt Body Wake Flow Measurement and Prediction Issues

High-temperature effects aside, accurate, quantitative measurement and numerical simulation of laminar, transitional, and turbulent separated/reattaching flows remains a challenge. Because of the operating range of most continuum hypersonic facilities, maintaining a laminar shear layer in regions of strong expansion (such as that encountered in the near wakes of blunt bodies) has in the past proven difficult.[14,15] In addition, the influence of a model support system are not well characterized, and the effects of tunnel noise on shear layer transition is not well understood. When turbulent interactions are present, numerical turbulence models play a crucial role in the simulation of these nonlaminar flows where separation, shock/boundary-layer interaction, and flow reattachment are present.[27] For the simpler laminar interactions, which avoid turbulence modeling, grid issues related to resolving near-wake flow features such as the free shear layer persist.[16]

The present experiments were performed in an effort to provide benchmark data for complex laminar/turbulent separated flows. Initial comparison of predicted laminar MSRO afterbody heating to experimental measurement did not capture the impingement heating peak observed experimentally.[11] The grid used in the wind-tunnel numerical simulation reported in Refs. 11 and 41 was adapted from a mesh utilized for obtaining flight predictions. This modified grid actually had finer resolution in the near wake relative to that used for the flight cases. Consistent to the flight prediction methodology, no attempt was made to align the grid with the wake shear layer. Thus, in contrast to the experimental results, a broad heating plateau was predicted near impingement, in part, due to numerical diffusion of the shear layer. In an attempt to assess the sensitivity of wake closure characteristics and shear layer diffusion to grid alignment, a second calculation was made[42] with the wake grid realigned with wake streamlines. In that study, the realigned grid reduced the level of numerical shear layer diffusion and produced a sharper heating increase at the location of predicted flow impingement.

The rapid expansion of the flow around the MSRO shoulder and subsequent reattachment on the afterbody has the potential to produce low wake densities with strong gradients. If these density gradients occur over distances that are small compared to the local flow mean free path, flowfield computations with Navier–Stokes methods may incur inaccuracies. When this situation occurs, the continuum assumptions on which the Navier–Stokes equations are based break down. Such flows typically have significant velocity slip along wall boundaries and a high degree of nonequilibrium between the translational modes, as well as the internal degrees of freedom. These effects can produce significant errors in the Navier–Stokes modeling of viscous transport properties that are particularly important to the numerical calculations of the wake shear layer and reattachment shock. The predicted Knudsen numbers reported in Ref. 42 indicated regions of noncontinuum flow downstream of the flow separation at the MSRO shoulder and in the reattachment shock region on the afterbody. The presence of these regions suggested that the original Navier–Stokes prediction reported in Refs. 11 and 41 may have incurred errors in the numerical calculation of the wake shear layer development and impingement due to noncontinuum effects. As a result, a three-dimensional coupled computational fluid dynamics (CFD) direct simulation Monte Carlo (DSMC) solution method was implemented in Ref. 43 in an attempt to further resolve differences between blunt-body near-wake heating measurement and prediction. Improvements in comparisons with measurement were noted with this coupled computational strategy (relative to those obtained with CFD alone) and it was suggested in Ref. 43 that the CFD–DSMC approach may be a more suitable method to obtain a higher fidelity wake solution should local noncontinuum regions exist in the near wake of a blunt body.

Conclusions

The NASA LaRC 20-Inch Mach 6 Air and CF_4 tunnels were used to assess the afterbody heating characteristics of a proposed MSRO. The Mach 6 CF_4 tunnel utilizes a heavy gas (CF_4) to generate a higher value of normal shock density ratio (than can be achieved in air tunnels), which is more appropriate in simulation of hypervelocity flight through planetary or Earth atmospheres. The purpose of the present study was to develop a benchmark experimental surface heating database for comparison of near-wake prediction to measurement under laminar, transitional, and turbulent perfect gas conditions. A secondary objective was to investigate the near-wake closure characteristics of the proposed European MSRO vehicle, to determine if shear layer impingement would occur on the MSRO afterbody at incidence angles appropriate to an aerocapture maneuver, and, if present, to determine the location and magnitude of the heating peak for laminar and nonlaminar interactions. Global heat transfer mappings, surface streamline patterns, and shock shapes were obtained for postnormal shock Reynolds numbers (based on forebody diameter) ranging from 1.42×10^3 to 4.15×10^5, angles of attack ranging from -5 to 10 deg at 0-, 3-, and 6-deg sideslip, and normal shock density ratios of 5 and 12.

The present MSRO laminar data are consistent with a previously developed correlation for blunt-body wake shear layer turning and have suggested the general applicability of the correlation in providing initial design estimates defining the usable volume for payload placement behind an aerobrake. Based on the present measurements, a nonlaminar wake shear layer (transitional or turbulent) is inferred for $Re_{2D} > 3.946 \times 10^3$ and produces a larger shear layer turning angle (relative to a laminar counterpart). Laminar, transitional, and turbulent shear layer impingement on the cylindrical afterbody resulted in a localized heating maximum that ranged from 40 to 75% of the reference forebody stagnation point heating. In perspective, the postnormal shock Reynolds number for Mars entry at peak heating conditions is expected to be near $Re_{2D} = 8.3 \times 10^4$. Although the shear layer transition onset Reynolds number should not be applied directly to flight due primarily to the adverse effect of tunnel noise, the ground-based measurements are considered conservative and suggest the possibility of a nonlaminar wake during the aerocapture maneuver (particularly if transition is initiated via forebody surface ablation or roughness).

Reynolds number and MSRO baseplane geometry (open and closed) have a pronounced effect on the magnitude of the nondimensional peak heating associated with shear layer impingement on the MSRO afterbody. For a laminar wake condition ($Re_{2D} < 3.946 \times 10^3$) in $M_\infty = 6$ CF_4 at $\alpha = -4$ deg, the peak heating associated with the closed baseplane is approximately 60% lower relative to that obtained with the open base (from $h/h_{\text{ref}} = 0.43$ to 0.27). For both base geometries, a nonlaminar base flow ($Re_{2D} > 3.946 \times 10^3$) produces a linear increase in reattachment heating with the log of the postshock Reynolds number based on body diameter. Curve fits to the data plotted in semilog form indicate the rate change of normalized peak heating associated with the closed base is approximately twice that of the open base. Thus, in contrast to the laminar situation, a turbulent wake in $M_\infty = 6$ air ($Re_{2D} = 4.15 \times 10^5$) produces afterbody peak heating associated with the closed baseplane that is approximately 23% higher than that measured with the open base (from $h/h_{\text{ref}} = 0.73$ to 0.90). The turbulent wake associated with the closed MSRO base represents a worst-case scenario in terms of afterbody heating where localized values at reattachment approached forebody stagnation levels.

Acknowledgments

Without the assistance of the following individuals, this work would not have been possible: Mark Cagle, Chris Glass, Joe Powers, Mike Powers, Mark Griffith, Steve Nevins, Gary Waynewright, and

Ed Covington for model design, fabrication, and instrumentation; Melanie Lawhorne, Harry Stotler, Crystal Kellam, Al Garner, John Ellis, Grace Gleason, Rowland Hatten, and Steve Jones for wind-tunnel support; Sheila Wright, Bert Senter, and Mike Difulvio for data acquisition assistance; Scott Berry and Brian Hollis for analysis support; Peter Gnoffo for computational fluid dynamics analysis support; and Richard Wheless for documentation assistance. The authors gratefully acknowledge their contributions and behind-the-scenes work.

References

[1]Smith, B. A., "Lander Development Paced By Mars Science Results," *Aviation Week and Space Technology*, Vol. 152, No. 26, 2000, p. 63.

[2]Smith, B. A., "NASA Weighs Mission Options," *Aviation Week and Space Technology*, Vol. 153, No. 24, 2000, p. 54.

[3]Pieri, D., "Rebuilding the U.S. Mars Exploration Program," *Launchspace*, July/Aug. 2000, p. 27.

[4]Taverna, M. A., "Europe to have Major Sample Return Role," *Aviation Week and Space Technology*, Vol. 153, No. 24, 2000, p. 60.

[5]Williams, S. D., "A Preliminary TPS Design for MRSR-Aerobraking at Mars and at Earth," AIAA Paper 90-0052, Jan. 1990.

[6]Meyerson, R. E., and Cerimele, C. J., "Aeroassist Vehicle Requirements for a Mars Rover/Sample Return Mission," AIAA Paper 88-0303, Jan. 1988.

[7]Gamble, J. D., "JSC Pre-Phase-A Study Mars Rover Sample Return Mission Aerocapture, Entry, and Landing Element," NASA Johnson Space Center, JSC-23230, May 1989.

[8]Mitcheltree, R. A., Kellas, S., Dorsey, J. T., Desai, P. N., and Martin, C. J., "A Passive Earth-Entry Capsule for Mars Sample Return," AIAA Paper 98-2851, June 1998.

[9]Amundsen, R. M., Dec, J. A., Mitcheltree, R. A., Lindell, M. C., and Dillman, R. A., "Preliminary Thermal Analysis of a Mars Sample Return Earth Entry Vehicle," AIAA Paper 2000-2584, June 2000.

[10]Glass, C. E., and Gnoffo, P. A., "A 3-D Coupled CFD-DSMC Solution Method With Application to the Mars Sample Return Orbiter," *22nd International Symposium on Rarified Gas Dynamics*, American Inst. of Physics, Melville, NY, 2000.

[11]Gnoffo, P. A., "Computational Aerothermodynamics in Aeroasist Applications," *Journal of Spacecraft and Rockets*, Vol. 40, No. 3, 2003, pp. 305–311.

[12]Chanetz, B., "Study of the Mars Sample Return Orbiter in the Hypersonic Wind Tunnel R5Ch," *Proceedings of the Atmospheric Reentry Vehicle and Systems Symposium*, French Association for Aeronautics and Astronautics, 1999.

[13]Gnoffo, P. A., "Planetary-Entry Gas Dynamics," *Annual Review of Fluid Mechanics*, Vol. 31, 1999, pp. 459–494.

[14]Horvath, T. J., McGinley, C. B., and Hannemann, K., "Blunt Body Near Wake Flow Field at Mach 6," AIAA Paper 96-1935, June 1996.

[15]Horvath, T. J., and Hannemann, K., "Blunt Body Near Wake Flow Field at Mach 10," AIAA Paper 97-0986, Jan. 1997.

[16]Hollis, B. R., "Experimental and Computational Aerothermodynamics of a Mars Entry Vehicle," NASA CR 201633, Dec. 1996.

[17]Wells, W. L., "Measured and Predicted Aerodynamic Heating on a Cylinder in Wake of AFE Configuration at Incidence," AIAA Paper 89-2162, 1989.

[18]Jones, R. A., and Hunt, J. L., "Use of Tetrafluoromethane to Simulate Real-Gas Effects on the Hypersonic Aerodynamics of Blunt Bodies," NASA TR R-312, 1969.

[19]Midden, R. E., and Miller, C. G., III, "Description and Calibration of the Langley Hypersonic CF4 Tunnel, A Facility for Simulating Low Gamma Flow as Occurs for a Real Gas," NASA TP 2384, Oct. 1985.

[20]Cheatwood, F. M., DeJarnette, F. R., and Hamilton, H. H., II, "Geometrical Description for a Proposed Aeroassist Flight Experiment Vehicle," NASA TM-87714, July 1986.

[21]Buck, G. M., and Vasquez, P., "An Investment Ceramic Slip-Casting Technique for Net-Form, Precision, Detailed Casting of Ceramic Models," U.S. Patent 5,266,252, 30 Nov. 1993.

[22]Merski, N. R., "Global Aeroheating Wind-Tunnel Measurements Using Improved Two-Color Phosphor Thermography Method," *Journal of Spacecraft and Rockets*, Vol. 36, No. 2, 1998, pp. 160–170.

[23]Miller, C. G., "Langley Hypersonic Aerodynamic/Aerothermodynamic Testing Capabilities—Present and Future," AIAA Paper 90-1376, June 1990.

[24]Merski, N. R., "Reduction and Analysis of Phosphor Thermography Data With the IHEAT Software Package," AIAA Paper 98-0712, Jan. 1998.

[25]Horvath, T. J., Berry, S. A., Hollis, B. R., Liechty, D. S., and Merski, N. R., "X-33 Experimental Aeroheating at Mach 6 Using Phosphor Thermography," *Journal of Spacecraft and Rockets*, Vol. 38, No. 5, 2001, pp. 634–645.

[26]Berry, S. A., Bouslog, S. A., Brauckmann, G. J., and Caram, J. M., "Shuttle Orbiter Experimental Boundary-Layer Transition Results with Isolated Roughness," *Journal of Spacecraft and Rockets*, Vol. 35, No. 3, 1998, pp. 241–248.

[27]Horvath, T. J., Berry, S. A., Merski, N. R., and Fitzgerald, S. M., "X-38 Experimental Aerothermodynamics," *Journal of Spacecraft and Rockets*, Vol. 41, No. 2, 2004, pp. 272–292.

[28]Fay, J. A., and Riddell, F. R., "Theory of Stagnation Point Heat Transfer in Dissociated Air," *Journal of Aeronautical Sciences*, Vol. 25, No. 2, 1958, pp. 73–85.

[29]Wuerer, J. E., and Clayton, F. I., "Flow Separation in High-Speed Flight, A Review of the State-of-the-Art," Douglas Aircraft Co., Inc., Rept. SM-46429, Santa Monica, CA, April 1965.

[30]Baker, P. J., and Martin, B. W., "Heat Tranfer in Supersonic Separated Flow Over a Two-Dimensional Backward Facing Step," *International Journal of Heat and Mass Transfer*, Vol. 9, Oct. 1966, pp. 1081–1088.

[31]Nance, R. P., and Horvath, T. J., "Transition and Turbulence Modeling for Blunt-Body Wake Flows," AIAA Paper 97-2570, June 1997.

[32]Berger, S. A., *Laminar Wakes*, American Elsevier, New York, 1971.

[33]Lees, L., "Hypersonic Wakes and Trails," *AIAA Journal*, Vol. 2, No. 3, 1964, pp. 417–428.

[34]Zeiberg, S. L., "Transition Correlations for Hypersonic Wakes," *AIAA Journal*, Vol. 2, No. 3, 1964, pp. 564, 565.

[35]Gnoffo, P. A., Price, J. M., and Braun, R. D., "Computation of Near-Wake Aerobrake Flowfields," *Journal of Spacecraft and Rockets*, Vol. 29, No. 2, 1992, pp. 182–189.

[36]Haney, J. W., "Orbiter Pre STS-1 Aeroheating Design Data Base Development Methodology: Comparison of Wind Tunnel and Flight Test Data," *Orbiter Experiments (OEX) Aerothermodynamics Symposium*, NASA CP-3248, Pt. 2, 1995, pp. 607–676.

[37]Jones, J. J., "The Rationale for an Aeroassist Flight Experiment," AIAA Paper 87-1508, June 1987.

[38]Brauckmann, G. J., Paulson, J. W., and Weilmuenster, J. K., "Experimental and Computational Analysis of Shuttle Orbiter Hypersonic Trim Anomaly," *Journal of Spacecraft and Rockets*, Vol. 32, No. 5, 1995, pp. 758–764.

[39]Giraud, S. P., "Investigation of the MSRO Heat Flux Distribution at the VKI Longshot Facility," von Kármán Inst., MARS-TN-MSRO-001-VKI, Feb. 2001.

[40]Dogra, V. K., Moss, J. N., Wilmoth, R. G., Taylor, J. C., and Hassan, H. A., "Effects of Chemistry on Blunt-Body Wake Structure," *AIAA Journal*, Vol. 33, No. 3, 1995, pp. 463–469.

[41]Horvath, T. J., Heiner, N. C., Olguin, D. M., Cheatwood, F. M., and Gnoffo, P. A., "Afterbody Heating Characteristics of a Proposed Mars Sample Return Orbiter," AIAA Paper 2001-3068, June 2001.

[42]Horvath, T. J., Cheatwood, F. M., Wilmoth, R. G., and Alter, S. J., "Wake Closure Characteristics and Afterbody Heating On a Mars Sample Return Orbiter," *Innovative Transportation Systems for Exploration of the Solar System and Beyond. STAIF /AIP Conference Proceedings*, Vol. 608, American Inst. of Physics, Melville, NY, 2002, pp. 318–336.

[43]Glass, C. A., and Horvath, T. J., "Comparison of a 3-D CFD-DSMC Solution Methodology with a Wind Tunnel Experiment," NASA TM-2002-21777, Aug. 2002.

B. Hassan
Associate Editor